Terahertz wavefronts measured using the Hartmann sensor principle

M. Cui,[1,2,*] J. N. Hovenier,[2] Y. Ren,[2,3,4] A. Polo,[5] and J. R. Gao[1,2]

[1] *SRON Netherlands Institute for Space Research, Sorbonnelaan 2, 3584 CA Utrecht, The Netherlands*
[2] *Kavli Institute of NanoScience, Delft University of Technology, Lorentzweg 1, 2628 CJ Delft, The Netherlands*
[3] *Purple Mountain Observatory (PMO), Chinese Academy of Science, 2 West Beijing Road, Nanjing, JiangSu 210008, China*
[4] *Graduate School, Chinese Academy of Sciences, 19A Yu Quan Road, Beijing 100049, China*
[5] *Optics Research Group, Department. of Imaging Science & Technology, Delft University of Technology, Lorentzweg 1, 2628 CJ Delft, The Netherlands*
**m.cui@tudelft.nl*

Abstract: We demonstrate for the first time that the Hartmann wavefront sensor (HWS) principle can be applied for characterizing the wavefronts of terahertz (THz) electromagnetic radiation. The THz Hartmann wavefront sensor consists of a metallic plate with an array of holes and a two-dimensional scanable pyro-electric detector. The THz radiation with different wavefronts was generated by a far-infrared gas laser operated at 2.5 THz in combination with a number of objects that result in known wavefronts. To measure the wavefront, a beam passing through an array of holes generates intensity spots, for which the positions of the individual spot centroids are measured and compared with reference positions. The reconstructed wavefronts are in good agreement with the model expectations.

OCIS codes: (040.2235) Far infrared or terahertz; (100.5070) Phase retrieval.

References and links

1. E. N. Leith, J. Upatnieks, and K. A. Haines, "Microscopy by wavefront reconstruction," J. Opt. Soc. Am. **55**(5), 981–986 (1965).
2. M. Schrader and S. W. Hell, "Wavefronts in the focus of a light microscope," J. Microsc. **184**, 143–148 (1996).
3. S. De Nicola, P. Ferraro, A. Finizio, and G. Pierattini, "Wave front reconstruction of Fresnel off-axis holograms with compensation of aberrations by means of phase-shifting digital holography," Opt. Lasers Eng. **37**(4), 331–340 (2002).
4. L. J. Golden, "Wavefront error simulator for evaluating optical testing instrumentation," Appl. Opt. **14**(11), 2756–2761 (1975).
5. J. M. Beckers, "Adaptive optics for astronomy: principles, performance, and applications," Annu. Rev. Astron. Astrophys. **31**(1), 13–62 (1993).
6. J. Liang, B. Grimm, S. Goelz, and J. F. Bille, "Objective measurement of wave aberrations of the human eye with the use of a Hartmann-Shack wave-front sensor," J. Opt. Soc. Am. A **11**(7), 1949–1957 (1994).
7. J. H. Bruning, D. R. Herriott, J. E. Gallagher, D. P. Rosenfeld, A. D. White, and D. J. Brangaccio, "Digital wavefront measuring interferometer for testing optical surfaces and lenses," Appl. Opt. **13**(11), 2693–2703 (1974).
8. C. Kulesa, "Terahertz spectroscopy for astronomy: From comets to cosmology," IEEE Trans. Terahertz Sci. Technol. **1**(1), 232–240 (2011).
9. C. B. Reid, E. Pickwell-MacPherson, J. G. Laufer, A. P. Gibson, J. C. Hebden, and V. P. Wallace, "Accuracy and resolution of THz reflection spectroscopy for medical imaging," Phys. Med. Biol. **55**(16), 4825–4838 (2010).
10. P. F. Taday, "Applications of terahertz spectroscopy to pharmaceutical sciences," Philos. Transact. A Math. Phys. Eng. Sci. **362**(1815), 351–364 (2004).
11. A. Bitzer, H. Helm, and M. Walther, "Beam-profiling and wavefront-sensing of THz pulses at the focus of a substrate-lens," IEEE J. Sel. Top. Quantum Electron. **14**(2), 476–481 (2008).
12. B. S. Williams, "Terahertz quantum-cascade lasers," Nat. Photonics **1**(9), 517–525 (2007).
13. B. C. Platt and R. Shack, "History and principles of Shack-Hartmann wavefront sensing," J. Refract. Surg. **17**(5), S573–S577 (2001).
14. H. I. Campbell and A. H. Greenaway, "Wavefront sensing: From historical roots to the state of the art," Astronomy with High Contrast Imaging III **22**, 165–185 (2006).

#167585 - $15.00 USD Received 27 Apr 2012; revised 27 May 2012; accepted 29 May 2012; published 13 Jun 2012

15. R. Densing, A. Erstling, M. Gogolewski, H.-P. Gemünd, G. Lundershausen, and A. Gatesman, “Effective far infrared laser operation with mesh coupler,” Infrared Phys. **33**(3), 219–226 (1992).
16. W. H. Southwell, “Wave-front estimation from wave-front slope measurements,” J. Opt. Soc. Am. **70**(8), 998–1006 (1980).
17. J. Schwiegerling and E. DeHoog, “Problems testing diffractive intraocular lenses with Shack-Hartmann sensors,” Appl. Opt. **49**(16), D62–D68 (2010).
18. F. Castignoles, T. Lepine, P. Chavel, and G. Cohen, “Shack-Hartmann multiple spots with diffractive lenses,” Opt. Lett. **36**(8), 1422–1424 (2011).
19. K. D. Irwin and G. C. Hilton, “Cryogenic particle detection: transition-edge sensors,” Top. Appl. Phys. **99**, 64–149 (2005).
20. J. Zmuidzinas, “Superconducting microresonators: Physics and Applications,” Ann. Rev. Condens. Matter Phys. **3**(1), 169–214 (2012).
21. N. Oda, H. Yoneyama, T. Sasaki, M. Sano, S. Kurashina, I. Hosako, N. Sekine, T. Sudoh, and T. Irie, “Detection of terahertz radiation from quantum cascade laser using vanadium oxide microbolometer focal plane arrays,” Proc. SPIE **6940**, 69402Y, 69402Y-12 (2008).
22. M. I. Amanti, M. Fischer, G. Scalari, M. Beck, and J. Faist, “Low-divergence single-mode terahertz quantum cascade laser,” Nat. Photonics **3**(10), 586–590 (2009).
23. S. J. E. Radford, “Refractive pointing jitter at the Chajnantor plateau,” (2007, unpublished), see *http://wiki.astro.cornell.edu/twiki/pub/CCAT/CCAT_Memos/2007-09-06-pointing-fluctuations.pdf*.
24. S. Hadjiloucas, G. C. Walker, and J. W. Bowen, “Extending murty interferometry to the Terahertz part of the spectrum,” J. Phys. Conf. Ser. **307**, 012012 (2011).
25. Y. Wang, Z. Zhao, Z. Chen, L. Zhang, and J. Deng, “Surface profile measurement by terahertz interferometric phase imaging,” J. Phys. Conf. Ser. **276**, 012222 (2011).

1. Introduction

A wavefront is a surface of a propagating wave in space, where all points on the surface have the same phase. The wavefront is one of the fundamental properties for electromagnetic radiation, connecting strongly to a variety of applications such as microscopy [1,2], holography [3], optical testing [4], adaptive optics [5], ophthalmology [6], and interferometric metrology [7].

Electromagnetic radiation in the THz frequency range is a relatively new, active research area and has peculiar characteristics that make it suitable for various applications for which the optics and microwave techniques are often unable to apply [8–10]. Although there have been many publications on the properties of THz radiation, until now the THz wavefronts have been rarely studied except for the wavefronts of short THz pulses [11]. There are strong demands to know and understand the wavefronts in the following examples. First, the coupling efficiency of the radiation from a coherent source to an antenna coupled detector or detector array depends not only on the beam patterns, but also the wavefronts; Second, for a THz source, like a quantum cascade laser (QCL) [12], not only is the beam profile a crucial characteristic, but also the wavefront; Finally, for astronomic instruments many optical components such as lenses and reflecting mirrors are introduced into the optical paths, therefore spatial wavefront distortion of the beam can occur.

In this paper, we propose a technique used for optical wavelength to measure the wavefronts in the THz domain by adapting the Hartmann wavefront sensor (HWS) [13]. As demonstrated in optical wavelengths, the wavefronts can be measured with a number of wavefront sensing techniques [14]. Among them, a Shack-Hartmann wavefront sensor (SHWS) based on a microlens array is the most well-known and commonly used wavefront sensor today because of the advantages such as its wide dynamic range and ability to use either continuous or pulsed sources. SHWS is widely used for adaptive optics. We choose to adapt the HWS to measure THz wavefronts instead of the SHWS because the mask with an array of holes used for HWS is easy to fabricate and therefore it is a quick way to demonstrate this technique. We introduce a THz HWS by combining a metallic plate containing an array of holes with raster scanning of a pyro-electric detector. The latter is applied to measure the intensity pattern of the THz radiation through the mask. The wavefronts with different shape are produced by using a far-infrared gas laser operating at 2.5 THz in combination with complex lenses. We have shown that the wavefronts can be measured at the THz frequencies and can be well explained by model calculations.

2. Design of a THz Hartmann wavefront sensor

The HWS can measure the wavefront of light using an array of holes in an opaque mask. The measurement principle is as follows; an incident wavefront passing through the holes can create a spot field on the detection plane. The positions of the spot centroids are measured and their lateral displacements from their local optic axis determine the local slope (first derivative) of the wavefronts. In this way, the wavefront of the incident beam can be reconstructed.

To design a mask plate, we perform the simulations of a spot pattern for a beam passing through an array of holes by varying different inputs with regard to the diameter of holes (*d*), the periodicity (*p*), and the distance from the mask to the detection plane (*L*). We optimize designs by judging from the sensitivity and the dynamic range of the HWS. The former is the minimal slope of the wavefront one can measure, and the latter defines the maximal measurable slope of the wavefronts. In our simulation, the Hartmann mask plate is located in the plane at $z = 0$, with a transmission function $G(x,y)$. We define $G = 1$ within the holes and $G = 0$ in the area of outside the holes. The field distribution in the $z = 0$ plane behind the mask is given according to the following equation,

$$E(x,y,0) = U(x,y)G(x,y) \tag{1}$$

where $E(x,y,0)$ is the electric field across the plane at $z = 0$ and $U(x,y)$ is the complex electric field of the incident wave. The field distribution in the detection plane $E(x;y;L)$ that locates at a distance of L behind the mask is calculated by Fourier transformation,

$$\hat{E}(k_x,k_y,L) = \hat{E}(k_x,k_y,0)e^{ik_z L} \qquad k_z = \sqrt{k_0^2 - k_x^2 - k_y^2} \tag{2}$$

where $\hat{E}(k_x,k_y,0)$ and $\hat{E}(k_x,k_y,L)$ are the Fourier transforms of $E(x,y,0)$ and $E(x,y,L)$ respectively, and k_x and k_y are the spatial frequencies in the Fourier domain.

To optimize the mask design, our simulation is focused on the incident radiation that is a plane wave with a wavelength (λ) of 100 μm, corresponding to 3 THz. Figure 1 shows a simulated field of spots in intensity for three different hole array designs on a 16 mm × 16 mm opaque mask. The first mask, defined as Mask 1, has holes of $d = 1$ mm with a periodicity of $p = 3$ mm in both x and y directions. The simulated spot fields are shown for two cases with either $L = 5$ mm or $L = 7$ mm for the detection plane behind the mask in the first column respectively. As shown in these two sub-figures, each hole produces an own imaging spot. For the case of $L = 5$ mm, the intensity of the spots is still concentrated in each center. However, for $L = 7$ mm, all the spots are getting bigger and also the contrast becomes lower. The latter is originated from a combination of the diffraction and the interference due to the overlap of beams from adjacent holes. If L is chosen to be 9 mm, although it is not shown in the figure, all the spots are so blurry that all imaging spots are nearly overlapped with each other due to the diffraction and interference.

Mask 2 has holes of $d = 1$ mm and a separation of $p = 2$ mm.. As shown in the two sub-figures in the second column, the imaging spots are comparable with those using Mask 1 for L = 5, but become worse than what observed in Mask 1 if $L = 7$ with regard to the size of the spots and contrast. We now continue to look at the results calculated for Mask 3, which has holes of $d = 0.7$mm and a separation of $p = 2.1$mm. The simulated spots fields are shown in the third column. We find that in general the imaging spots become less clear and even become indistinguishable between two adjacent ones. Obviously, when the diameter of the holes and their distance become smaller, the effects of diffraction and interference start to dominate the imaging spot quality.

#167585 - $15.00 USD Received 27 Apr 2012; revised 27 May 2012; accepted 29 May 2012; published 13 Jun 2012

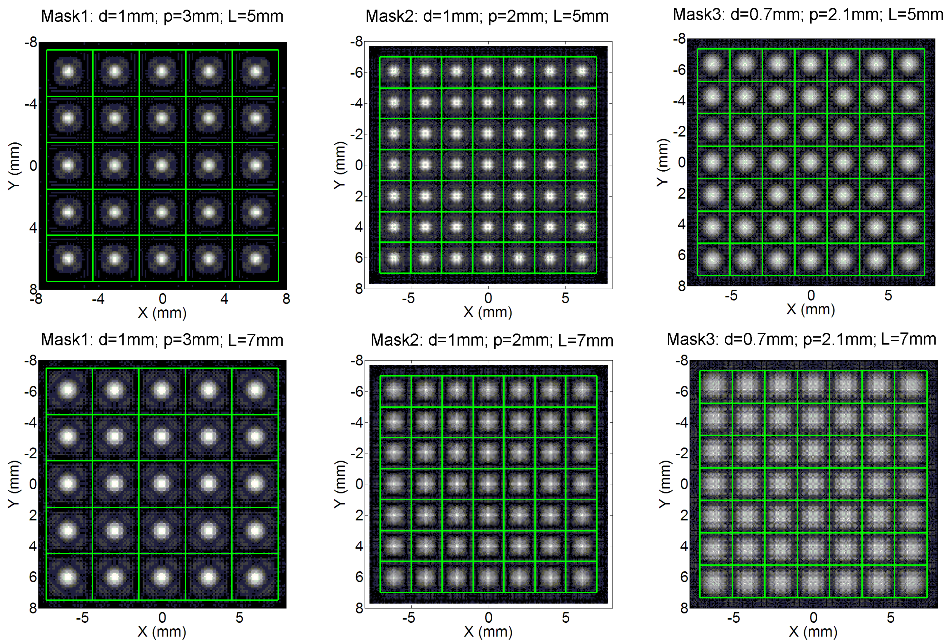

Fig. 1. Simulations of spot patterns for a THz radiation beam passing through an array of holes by varying the diameter of holes (d) and the periodicity (p) in three masks shown in the first column. The simulated spot fields on the detection plane that is 5mm and 7mm behind the mask are shown in the first and second row, respectively.

In order to determine the centriods of the imaging spots accurately, one needs smaller imaging spots and higher contrast. On the other hand, the sensitivity of the HWS is proportional to L since a large L can result in a large displacement of the imaging spot with respect to the reference. Therefore, our experiments start with Mask 1 with L = 7 mm.

3. THz Hartmann wavefront sensor and measurement setup

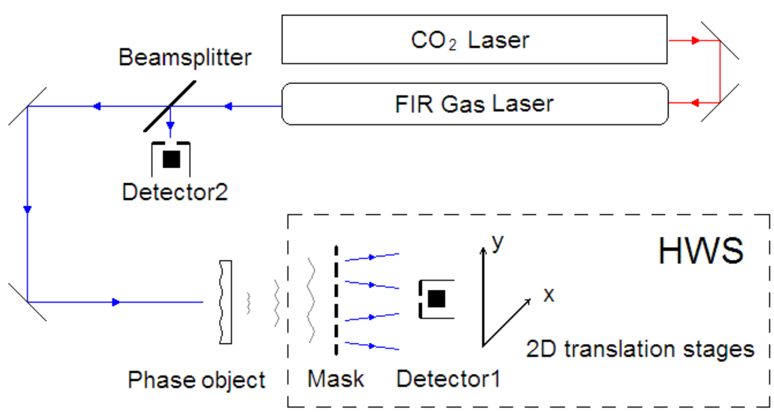

Fig. 2. Schematic of the measurement setup to demonstrate a THz Hartmann wavefront sensor (HWS). The beam generated from a FIR gas laser passes through a beam splitter. One part of the beam is monitored so that the change of the total power can been measured. Another part of the beam is reflected by two mirrors and shines onto the phase object. The HWS that contains a Hartmann mask and a pyro-electric detector on a 2D translation stage is used to measure the incident wavefront that is distorted by the phase object. The detector plane is located 7mm behind the Hartmann mask.

#167585 - $15.00 USD Received 27 Apr 2012; revised 27 May 2012; accepted 29 May 2012; published 13 Jun 2012

Figure 2 illustrates our experimental setup schematically. An optically pumped far-infrared (FIR) gas laser using methanol (CH_3OH) generates a radiation beam at 2.52 THz (corresponds to a λ of 119 μm) in our experiment. The cavity of the FIR gas laser is 1.5 meter long and the hole in the couplers is 10 mm in diameter. We choose the gas laser for testing the HWS since it has a Gaussian output beam and has a very low divergence as a result of large waist size [15]. The latter offers nearly an ideal planar wavefront. Furthermore, our gas laser has an output power of 20 mW at 2.5 THz, which allows the use of a pyro-electric detector whose sensitivity is relatively poor.

The gas laser beam, as shown in Fig. 2, is guided to the phase object by two flat mirrors. The phase object in our case is a high-density polyethylene (HDPE) lens that varies from a simple converging lens to a bi-focal lens that combines a converging one with a diverging one. The HDPE is chosen because of its low loss at THz frequencies. The phase object is to form a distorted, but predicable THz wavefront. Since the amplitude of the gas laser signal is not fully stable, we monitor the output power simultaneously by means of a second pyro-electric detector and beam splitter as shown in the same figure, which is used to correct the effect due to laser power draft to the imaging signal.

The Hartmann mask is based on the design of Mask 1, which consists of a 15 × 15 hole array, covering an area of 300 mm × 300 mm, made in a 0.2 mm thick copper plate. THz radiation can travel only through the holes, but not the copper plate since the skin depth in the copper at THz frequency is much smaller than 0.2 mm. Stycast, which is known to be an excellent THz radiation absorber, covers on the copper surface in order to minimize the reflection. The mask is mounted on a 2D translation stage. In order to increase the spatial resolution of the measured wavefront, we measure the field of the spots in such a way that we record the imaging in intensity by raster scanning of the detector across the beam in 2D on the optical axis, then shift the mask with a distance of 1 mm, for example, in the x-direction, then record the imaging again. For a complete wavefront measurement, we move the mask 9 times in both x and y–directions.

To obtain a field of spots in the detection plane, which we call the HWS spot field, we use the pyro-electric detector (Detector 1 in Fig. 2) with a NEP (Noise-equivalent power) of 5×10^{-9} $WHz^{-1/2}$ at 2.5 THz and with an input aperture of 1mm in diameter although the active area of the detector is 2 mm × 2 mm. The detector is mounted on a computer controlled 2D translation stage, which is driven at a speed of 1mm/sec. During the measurement the data sampling time interval is 100 msec. The distance between the mask and the detection plane is chosen at 7 mm. In this way, 200 × 200 resolution in the imaging can be obtained with a pixel size of 0.1mm × 0.1mm for a total area of 20 mm × 20 mm imaging area. Note that the resolution of the spot field is equivalent to the camera resolution for an HWS in the optical wavelengths. We now quantify the sensitivity and dynamic range for this specific arrangement. The sensitivity of the HWS is given by $\theta_{min} = \delta/L$, where δ = 0.1mm is the minimum detectable spot displacement and L = 7mm, resulting in a θ_{min} of 14 mrad. The dynamic range is given by $\theta_{max} = \Delta/L$, where Δ is the maximal measurable distance from the detected spot to the center of the grid. In our HWS, Δ = 1.5 mm and L = 7 mm, so θ_{max} = 0.2 rad.

#167585 - $15.00 USD Received 27 Apr 2012; revised 27 May 2012; accepted 29 May 2012; published 13 Jun 2012

4. Experiments

4.1. Planar wavefront

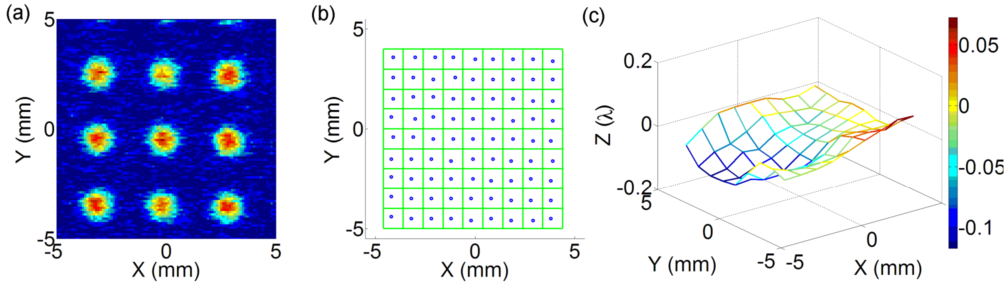

Fig. 3. (a) Directly measured spot field of the incident THz planar wavefront in the detection plane for a given Hartmann mask position; (b) the HWS spot field that consists of the extracted centriods of the imaging spots in (a), but measured by shifting the Hartmann mask by 1 mm in either x- or y-direction and in total 9 times. (c) The reconstructed wavefront from the centriods data in (b).

As the first step to calibrate the THz HWS, we measure the wavefront of the gas laser beam, directly passing through the Hartmann mask, without any phase object. The output beam of the gas laser has a divergent angle of 3.8 mrad, which is smaller than the sensitivity of our HWS (14 mrad), hence can be considered as planar wavefront. Figure 3(a) shows typical measured imaging spots in intensity at the detection plane. As mentioned previously, to complete a wavefront measurement, such imaging spots are measured 9 times with a 1 mm shift of the mask for each measurement. The centriods of the spots are determined. The resulted HWS spot pattern is plotted in Fig. 3(b), where each grid (green square) is a 1mm × 1mm square. For a perfect plane wave, the spots are expected to be located at the center of each grid. The obtained centriods are in practice deviated from the center of the grid within ± 0.2 mm in both x and y directions. The local slopes of the wavefront can be obtained from the spot field and the wavefront can be reconstructed from the local slopes by using Zonal wavefront estimation [16]. Before we comment on the deviations, we show in Fig. 3(c) a reconstructed wavefront based on the data in Fig. 3(b), which is close to a planar wavefront. However, the wavefront deviates from an ideal plane wave in a scale varying from -0.15λ to $+ 0.05\lambda$. Potential causes of the deviations are the followings. (a) During the measurement, the mask is aligned such that a row of holes is parallel to the horizontal scan of the detector. However, in practice, across the mask the misalignment can be about 0.1 mm. This may introduce about 0.1λ tilt of the measured wavefront with respect to the optical axis (the z-axis). (b) We assume the beam of the gas laser to be a perfect plane wave, but in reality there might also be local, tiny deviations in the wavefront.

#167585 - $15.00 USD Received 27 Apr 2012; revised 27 May 2012; accepted 29 May 2012; published 13 Jun 2012

4.2. Spherical wavefronts

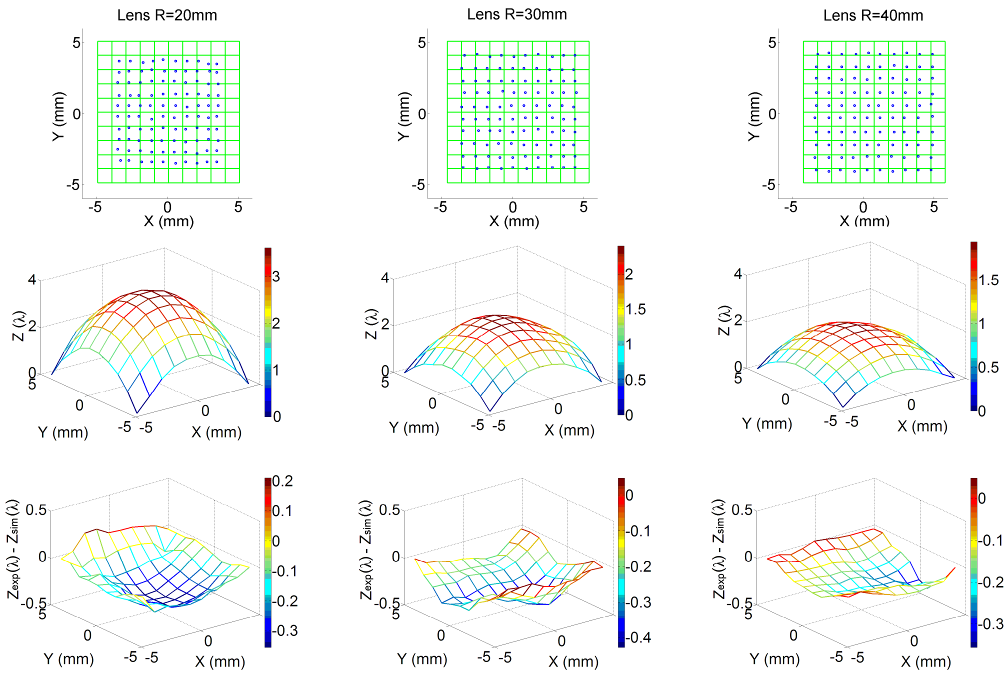

Fig. 4. In the first row: the HWS spot fields of spherical THz wavefronts generated by three lenses with different focal distance. The radii of curvature of the lenses are 20 mm (the first column), 30 mm (the second column) and 40 mm (the third column), respectively. In the second row: reconstructed wavefronts. In the third row: difference between measured wavefronts and perfect spherical wavefronts from a simulation.

To further characterize the HWS, spherical waves of different radii are generated using phase objects that are HDPE lenses with different focal distances. We use three plano-convex spherical lenses with radii of curvature of 20mm, 30mm, and 40mm, respectively. For this set of measurements, the mask was located 5 mm behind the lens (note this is different from L that is the distance between mask and detection plane). The choice of this distance is based on two practical considerations, namely enough space allowing displacing the mask and large enough beam (radiation imaging) on the mask. Applying the same procedure as for the plane wave, the centriods of the spots are determined for the three phase objects and are plotted in the first row in Fig. 4. The wavefronts are therefore reconstructed and are also plotted in the second row of Fig. 4. We compare our measured wavefronts to those simulated for perfect spherical waves using the expected radii, calculated based on the three nominal focal distances of the lenses. The difference between the reconstructed wavefront and the simulated wavefront, ($Z(\lambda)_{meas}$-$Z(\lambda)_{simu}$), is plotted in the third row of Fig. 4. The maximal difference (peak to peak) is found to be 0.5λ for the wavefront generated using the lens with a surface radius of 20 mm (the first column) and this difference decreases to about 0.3 λ for the lens with the largest surface radius.

To derive the radii of the measured wavefronts, we make use of the distance between two centriods of the adjacent spots since for an ideal spherical wave; this distance should be constant within the HWS spot pattern, leading to the radius of the wavefront. In Table 1 we listed the radii of the measured wavefronts and the ones calculated from the focal distances of the lenses. The measured radii are derived from the averaged spot separations, with uncertainties coming from the standard deviation of the measured spot separations from their averaging. We note that the radii measured on the x and y-axes should be equal, however, due to measurement uncertainty, they are not necessary to be exactly the same. This can be caused

#167585 - $15.00 USD Received 27 Apr 2012; revised 27 May 2012; accepted 29 May 2012; published 13 Jun 2012

by a couple of possible reasons, one of them being the small tilt of the mask. We find that the measured radii within the error bar agree reasonably well with the expected ones. For example, for the lens using a focal distance of 20 mm, the measured radius of the wavefront is equal exactly to what is expected.

Table 1. The focal distances of the lenses used to generate spherical wavefronts. The measured radius refers to the radius of a reconstructed wavefront, and the expected radius refers to the calculated radius.

Lens	R = 20mm	R = 30mm	R = 40mm
Measured radius (x)	33 ± 2mm	56 ± 5mm	72 ± 10mm
Measured radius (y)	33 ± 2mm	58 ± 5mm	80 ± 10mm
Expected radius	33mm	53mm	72mm

In addition to the two factors mentioned in the plane wavefront measurement, the following facts may influence the measured spherical wave and the related radius. (a) The distance between the mask to the detector in practice may have ± 0.5mm deviation from 7 mm, which can cause the deviations in the wavefront of 0.26λ (R = 20mm), 0.17λ (R = 30mm) and 0.14λ (R = 40mm). (b) There is possible mask tilting on the z-axis. The expected deviation is less than 0.2 mm, which may cause an error of ± 0.1λ on the wavefront. The errors taking (a) and (b) into account can roughly explain the deviations from an ideal spherical wavefront. (c) We use the nominal values of the focal distances of the HDPE lenses. However, in reality, 1~2 mm deviation from the designed focal distance is very likely. This may explain the slight difference between measurement and expectation.

4.3. Wavefronts generated by complex phase objects

We now exam the HWS by measuring the wavefronts generated by two complex phase objects. The first one, shown in Fig. 5(a), consists of a bi-focal HDPE lens that combines a convex lens in the center and a concave lens on the edge. The inner lens has a diameter of 10 mm and the outer lens has a diameter of 25 mm. The radii of the two lenses are both 30 mm. Before measuring the wavefront, the intensity distribution or beam pattern after the lens is measured within a 20 mm × 20 mm area and plotted in Fig. 5(b), where three distinguishable regions are the filled, highly intensive circle in the center, a ring with low intensity, and the rest with an intensity lying just between the two. Such an intensity profile is expected since when THz radiation passes through the inner lens there is converging of the radiation, while when the radiation passes through the outer lens it becomes diverging. The ring in Fig. 5(b) is formed around the transition region caused by the two lenses.

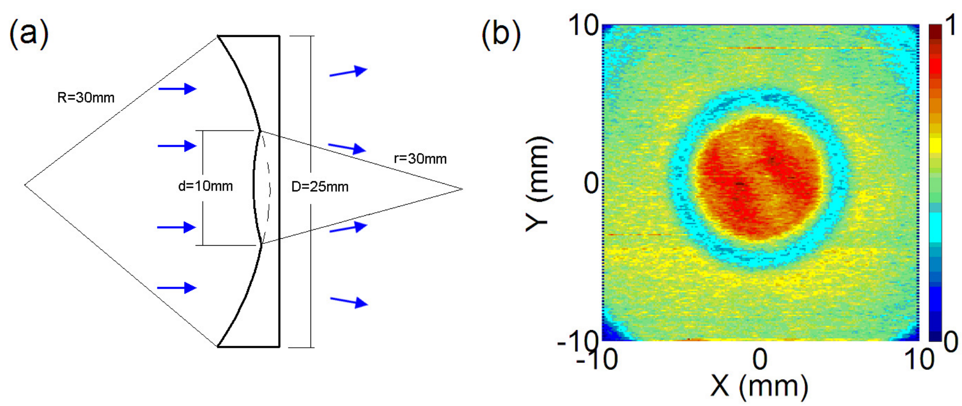

Fig. 5. (a) HDPE lens that combines a convex lens in the center with a concave lens on the edge functions as the first complex phase object. (b) The intensity distribution at the detection plane behind the phase object, measured without the Hartmann mask.

#167585 - $15.00 USD Received 27 Apr 2012; revised 27 May 2012; accepted 29 May 2012; published 13 Jun 2012

With the HWS mask, the centriods of the spots in a 17 × 17 pixel image with a spatial resolution of 1 mm × 1 mm are determined and plotted in Fig. 6(a). The black circle in the figure marks the transition between the inner lens and the outer lens. The spots corresponding to the radiation wavefront from the inner lens are drawn in red and the spots from the outer lens are drawn in blue. The spots near the transition ring, if connected one by one either in x-direction or in y-direction, are curved, suggesting a clear change of the direction of the wavefront. The reconstructed wavefront that has a Mexican-hat shape with a maximum in the center and a minimum along the transition ring is shown in Fig. 6(b). We find that the radius of the measured wavefront corresponding to the inner lens is 54 ± 4mm, averaged from the measured values in both x and y directions. This is in good agreement with the expected wavefront radius that is 53mm. A similar agreement appears for the outer lens, where the measured wavefront radius is 68 ± 8mm, while the expected wavefront radius is 65mm.

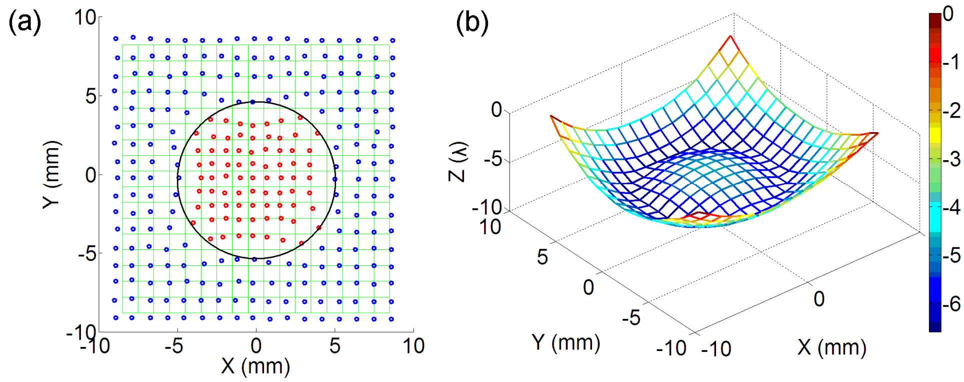

Fig. 6. (a) HWS spot field of the THz wavefront generated by the first complex phase object described in Fig. 5. The black circle indicates the transition region from the inner lens to the outer lens. The spots coming from the inner lens are drawn in red and the spots from the outer lens are drawn in blue. (b) The reconstructed wavefront from (a).

The second complex phase object is also a bi-focal lens, but being the inverse of the first one. As shown in Fig. 7(a), its center is a concave lens and the outer is a convex one. The radiation passing through the inner lens becomes diverging, while the radiation through the outer lens becomes converging. Interestingly there will be a ring-like zone where the (coherent) radiation beams from two different lenses intercept and form interference patterns. The intensity distribution after the 2nd phase object, but without HWS mask, is measured and shown in Fig. 7(b). As expected, no interference pattern is observed in the center and the outer. However, interference patterns characterized by a set of rings with maxima and minima in intensity are observed in the zone where two radiation beams are overlapped.

#167585 - $15.00 USD Received 27 Apr 2012; revised 27 May 2012; accepted 29 May 2012; published 13 Jun 2012

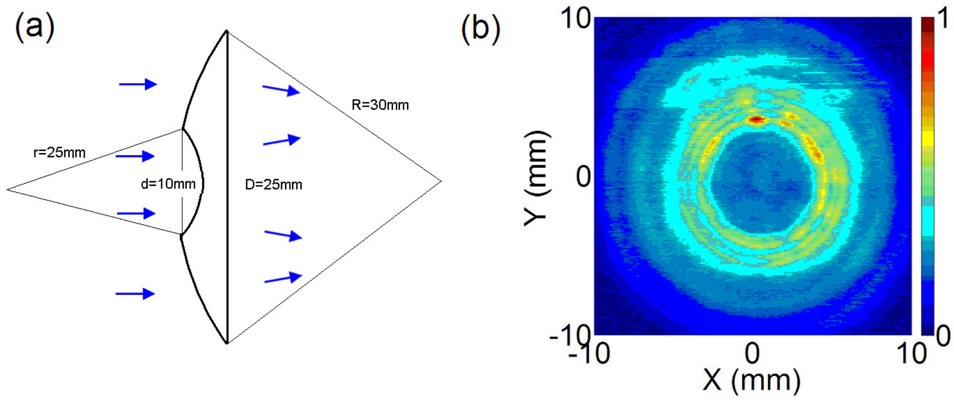

Fig. 7. (a) HDPE lens that combines a concave lens in the center with a convex lens on the edge acts as the 2nd complex phase object. (b) The intensity distribution at the detection plane behind the phase object, measured without the Hartmann mask.

The measured spot pattern is shown in Fig. 8(a). In the central and outer regions of the measured spot field, usual single spots have been observed. However, in the zone where the interference pattern appears, two independent spots formed by the beams from the inner and outer lenses, through a single hole in the mask, are captured. A similar phenomenon has been reported for the wavefronts of the optical light (λ = 550 nm), which is generated by multi-focal diffractive lenses, measured using a SHWS [17, 18]. However, this is the first time that this effect has been observed at the THz wavelengths with a HWS. The physics is very straightforward and is related to the two beams with different wavefronts. To emphases these double-spots, we draw a black line across each two spots originated from the same hole in the mask. Since the HWS measures only the slope of the wavefront, this method is in principle unable to determine discontinuous wavefronts. In order to make use of those two spots, we calculate the weighted centers of each two and also use them to construct a continuous wavefront. The result is shown in Fig. 8(b).

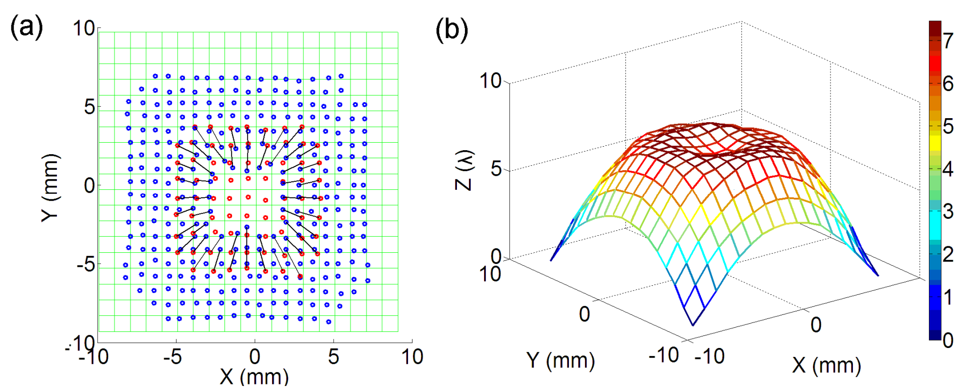

Fig. 8. (a) HWS spot field of the THz wavefront generated by the second complex phase object described in Fig. 7. The red spots originated from the inner lens and the blue ones from the outer lens. The two spots coming from the same hole are connected by a black line. (b) The reconstructed wavefront from (a). The weighted centers of each two spots connected through a black line are used to construct a continuous wavefront.

We find that the radius of the measured wavefront corresponding to the inner lens is 53 ± 4mm, averaged from the measured value in both x and y direction. The expected radius from the inner lens is 53 mm so the agreement is excellent. A similar agreement appears for the

#167585 - $15.00 USD Received 27 Apr 2012; revised 27 May 2012; accepted 29 May 2012; published 13 Jun 2012

outer lens, where the measured wavefront radius is 52 ± 3mm and the expected wavefront radius is 53mm.

5. Discussions

Our experiment is the first attempt to measure the wavefront of CW radiation at THz wavelengths. Compared to those in the visible and near infrared wavelengths, the HWS in the THz domain can be further improved in a few aspects.

One possible improvement is to replace the HWS by a SHWS based on a microlens array. Each lens can be made of a low loss and low reflective index material such as HDPE and has a small diameter of, e.g. 1~2 mm. The advantages of using the SHWS are the following: First, the total number of the spots can be increased by enlarging the beam. In our experiment, we have recorded a 9 × 9 spot array for planar and spherical wavefronts and a 17 × 17 spot array for the complex wavefronts. The total spot number is limited by the size of the holes, which can't be much smaller than 10λ because of the diffraction. Enlarging a beam will certainly increase the total number of the spots, but also decrease the intensity of each spot. If the spots are focused by lenses, then the intensity of the focused spot could be higher, hence can be distinguished with less incident power. Second, the mask needn't be moved and the measurement time can be reduced. When the holes are changed into lenses, the focused spots are smaller and easier to be determined. The same spatial resolution as of the HWS can be achieved without moving the mask if all the microlenses are closely packed.

Another improvement is to use sensitive multi-pixel THz camera instead of a single-pixel pyroelectric detector. As it is now, recording a 9 × 9 HWS spot pattern requires about 3 hours and recording a 17 × 17 spot pattern takes 10 hours. Such long measurement time is mainly caused by the time needed for a 2D raster scan using a single-pixel detector. Furthermore, the THz detector used in this experiment has a relatively poor sensitivity. This issue can be solved by introducing a sensitive multi-pixel THz camera. The THz camera based on superconducting detectors such as transition edge sensors (TES) [19] and kinetic inductance detectors (KIDs) [20] with a NEP below $10^{-17}\mathrm{WHz}^{-1/2}$ have already been developed for astronomic applications although in our case there is no need for so extremely low NEP. THz cameras operated at room temperature are also in progress and some of them have already been demonstrated in the laboratories with a NEP of $4 \times 10^{-11}\mathrm{WHz}^{-1/2}$ at 3.1 THz [21]. By introducing a THz camera into a SHWS, the measurement efficiency can be improved drastically, thus the speed will not be an issue anymore.

6. Summary

We succeed in demonstrating a Hartmann wavefront sensor to characterize the wavefront of THz electromagnetic radiation. The HWS consists of a metallic hole array mask and a pyro-electric detector. Different wavefronts of the THz radiations generated by a far-infrared gas laser at 2.5 THz in combination with mono-focal and bi-focal lenses are measured and reconstructed. They show in general excellent agreement with the calculations. We have also applied our HWS to measure the wavefront of a 3rd order distributed feedback (DFB), 3.5 THz quantum cascade laser [22]. Good spherical wavefront has been obtained and the detailed analysis of the data in relation with the laser structure is in progress. Although this new technique at THz frequencies still needs to be improved, the Hartmann wavefront sensor is a very promising technique for numerous potential applications. For example, it can be used for determining different wavefront of a THz radiation source, such as a THz quantum cascade laser, allowing characterizing not only the beam pattern but also the wavefront of a new laser. Since a new generation of ground based large telescopes for sub-millimeter astronomy are coming into service, adaptive optics techniques can be used to improve the performance of optical systems by reducing the effect of wave front distortion, caused by fluctuations in atmospheric refraction [23]. Also the wavefront sensor can be used in material testing [24] and surface profile measurement [25] in the THz region since all these techniques

#167585 - $15.00 USD Received 27 Apr 2012; revised 27 May 2012; accepted 29 May 2012; published 13 Jun 2012

are based on the measurement of the wavefront distortion induced by passing through a sample or reflecting from a distorted surface.

Acknowledgment

The authors acknowledge T.M. Klapwijk for his helpful discussions. The authors thank M. Popinciuc for his help on the Labview measurement program. The work was supported by NWO, KANW China Exchange Programme, TeraDec, and NATO SfP.

#167585 - $15.00 USD Received 27 Apr 2012; revised 27 May 2012; accepted 29 May 2012; published 13 Jun 2012